OPEN ACCESS
IOP Publishing | IMMT
International Journal of Extreme Manufacturing
Int. J. Extrem. Manuf. 7 (2025) 015601 (17pp)
https://doi.org/10.1088/2631-7990/ad870e

Quasi-visualizable detection of deep sub-wavelength defects in patterned wafers by breaking the optical form birefringence

Jiamin Liu[1], Jinlong Zhu[1,*], Zhe Yu[1], Xianrui Feng[1], Zedi Li[1], Lei Zhong[1], Jinsong Zhang[1], Honggang Gu[1], Xiuguo Chen[1], Hao Jiang[1,*] and Shiyuan Liu[1,2,*]

[1] State Key Laboratory of Intelligent Manufacturing Equipment and Technology, Huazhong University of Science and Technology, Wuhan 430074, People's Republic of China
[2] Optics Valley Laboratory, Wuhan 430074, People's Republic of China

E-mail: jinlongzhu03@hust.edu.cn, hjiang@hust.edu.cn and shyliu@hust.edu.cn

Received 29 February 2024, revised 16 May 2024
Accepted for publication 14 October 2024
Published 5 November 2024

Abstract

In integrated circuit (IC) manufacturing, fast, nondestructive, and precise detection of defects in patterned wafers, realized by bright-field microscopy, is one of the critical factors for ensuring the final performance and yields of chips. With the critical dimensions of IC nanostructures continuing to shrink, directly imaging or classifying deep-subwavelength defects by bright-field microscopy is challenging due to the well-known diffraction barrier, the weak scattering effect, and the faint correlation between the scattering cross-section and the defect morphology. Herein, we propose an optical far-field inspection method based on the form-birefringence scattering imaging of the defective nanostructure, which can identify and classify various defects without requiring optical super-resolution. The technique is built upon the principle of breaking the optical form birefringence of the original periodic nanostructures by the defect perturbation under the anisotropic illumination modes, such as the orthogonally polarized plane waves, then combined with the high-order difference of far-field images. We validated the feasibility and effectiveness of the proposed method in detecting deep subwavelength defects through rigid vector imaging modeling and optical detection experiments of various defective nanostructures based on polarization microscopy. On this basis, an intelligent classification algorithm for typical patterned defects based on a dual-channel AlexNet neural network has been proposed, stabilizing the classification accuracy of $\lambda/16$-sized defects with highly similar features at more than 90%. The strong classification capability of the two-channel network on typical patterned defects can be attributed to the high-order difference image and its transverse gradient being used as the network's input, which highlights the polarization modulation difference between different patterned defects more significantly than conventional bright-field

* Authors to whom any correspondence should be addressed.

Original content from this work may be used under the terms of the Creative Commons Attribution 4.0 licence. Any further distribution of this work must maintain attribution to the author(s) and the title of the work, journal citation and DOI.

© 2024 The Author(s). Published by IOP Publishing Ltd on behalf of the IMMT
2631-7990/25/015601+17$33.00

microscopy results. This work will provide a new but easy-to-operate method for detecting and classifying deep-subwavelength defects in patterned wafers or photomasks, which thus endows current online inspection equipment with more missions in advanced IC manufacturing.

Supplementary material for this article is available online

Keywords: defect inspection, form birefringence breaking, high order difference, anisotropic illumination modes, deep-subwavelength sensitivity, defect classification

1. Introduction

Integrated circuit (IC) manufacturing is a whole-process technology consisting of a series of critical processes such as photolithography, development, etching, ion implantation, chemical-mechanical planarization, deposition, and their repeated combination [1–4], which enables the transfer from the mask layout patterns to the bare silicon wafers and the final construction of a complete circuit chip. Benefiting from the direct products of IC manufacturing, such as IC chips and devices [5–8], which support the operation and development of modern society [9], they have been regarded as the core of the information industry and a key force leading a new round of technological revolution and industrial transformation. With advanced IC processes breaking through sub-14 nm nodes, the processes involved in chip manufacturing become more complex, precise, diverse, and multi-step [10], which makes random process deviations and environmental pollution extremely prone to occur throughout the IC manufacturing process [11, 12]. Correspondingly, killer defects such as bridging, cutting lines, particles, and holes are also prone to appear in IC nanostructures [12–14], substantially affecting IC chips' final performance and yield. Therefore, it is of great significance to accurately detect and strictly control defects in patterned wafers during advanced IC manufacturing.

Since these killer defects are minor down to $\lambda/10$ and dispersedly distributed throughout the entire 12-inch silicon wafer [10], defect inspection carried out at various process layers with requirements such as high sensitivity, high resolution, high speed, and non-invasiveness has become a commonly reached consensus in the semiconductor field [12]. Currently, mainstream chip fabs usually combine bright-field microscopes and review-type scanning electron microscopy (Review SEM) to inspect defects in the patterned wafers at advanced IC process nodes [15, 16]. The former conducts a rough inspection of defective areas, while the latter carefully identifies defect features. Due to the shortcomings of scanning electron microscopy, such as slow speed, limited field of view, and easy damage to samples by high-dose electron beams [17], this detection method's overall efficiency cannot meet the need for comprehensive detection of all process layers of the entire wafer. Optical inspection technology, typically such as a bright-field microscopes-based inspection platform, due to its intrinsic advantages such as non-destruction and high speed, has become the workhorse for inspecting the deep sub-wavelength defects in patterned wafers in both industry and academia [18–20]. Generally speaking, optical inspection methods can be categorized according to the measurand (i.e. the amplitude, the phase, and the polarization state of light), such as the amplitude-based bright- or dark-field microscopy [21, 22], the phase-based diffraction phase microscopy and phase contrast microscopy [23, 24], and the polarization-based Mueller matrix microscopy [25, 26]. Although optical inspection methods differ in the measurands, the conventional flowchart of defect inspection is quite similar, i.e. the identification of a defect can be achieved by subtracting the image of a defective area from that of a defect-free area [27]. The underlying physics is quite simple, i.e. the defects behave as perturbations in the patterned wafer, which alter the electromagnetic response of the regular background nanostructures locally [28, 29].

However, optical inspection methods, especially bright- or dark-field microscopy based on far-field imaging, cannot tell what the defect looks like if its size is much smaller than the well-known diffraction limit (DL) [30], due to the weak correlation between the defect's scattering cross-section and its morphology. Moreover, these methods also face a sharp drop in detection sensitivity when the defect size shrinks to the so-called deep sub-wavelength scale (namely, one- or two-dimensional sizes shrink to about $\lambda/10$) [14]. These drawbacks of conventional bright- or dark-field inspection platforms severely hinder them from distinguishing the killer defects from non-killer ones with sizes less than DL. As a result, the time-consuming e-beam inspection tool has to be pushed to the front to classify various defects. In fact, scanning near-field optical microscopy, stimulated emission loss microscopy, and stochastic optical reconstruction microscopy can realize a resolution much smaller than the DL of conventional bright- and dark-field microscopy [31–33], but they are either slow or destructive due to the scanning mode and fluorescent labeling. Diffraction phase microscopy has been applied to inspect deep sub-wavelength defects in the patterned wafer by combining a post-processing algorithm to cancel out the background pattern [34, 35]. Still, it has not yet been demonstrated that it is capable of classifying different types of defects. The interferometric cross-polarization detection scheme adopts the interference between a y-polarized reference field with shifted frequency and the cross-polarized scattering field to enable the background-free sensing of 10 nm gold nanoparticles at both visible and near-infrared wavelength [36, 37], but to date, it has only been experimentally validated for the detection of particles on bare wafers. Therefore, an optical detection

method that is capable of positioning and classifying sub-wavelength defects in a non-destructive, fast, label-free, convenient to be integrated, and simple mode is of great importance to the fabs and academia.

The polarization-dependent beat-frequency interference techniques mentioned above can enhance the off-diagonal signals in the scattering matrix of nanoparticles [37, 38], thus enabling a high signal-to-noise ratio and high sensitivity detection of 10 nm nanoparticles, which allows us to notice the polarization modulation behavior of the sample has a positive effect on the sensing of nanoscale perturbation. It is indeed beneficial for the visualizable detection of deep sub-wavelength objects by appropriately utilizing both the first and second-order transverse gradient (x-y plane) of the scattered field, which can be inferred from the reported optical pseudo-electrodynamic microscopy and epi-illumination diffraction phase microscopy [14, 34, 39]. Besides, the form-birefringence-based inspection method can extend the inspection sensitivity to identify the bridging defects in the 14 nm logic 2nd-generation FinFET transistors [40], in which the scattering intensity ratios I_y/I_x between Y-polarization and X-polarization illumination conditions have been used as the figure of merit for the inspection sensitivity. Meanwhile, considering that form birefringence is essentially the difference in refractive index between two orthogonal polarized light caused by the geometrical structure [41], some researchers have tried to use the self-assembled, periodic array of sub-wavelength defects created by laser writing to tune the intrinsic birefringence of sapphire [42]. These methods inspire us to explore the impact of polarization modulation and the transverse gradient of scattering field from the nanostructure on the detection and classification of sub-wavelength defects.

In this work, we report on a new but easy-to-operate optical inspection method based on the concept of form-birefringence-breaking imaging, which is capable of classifying various types of sub-wavelength defects in the far-field. The term 'form-birefringence-breaking' means that a nanoscale perturbation can alter the difference between the scattering behavior of nanostructure under X-polarized illumination and that under Y-polarized illumination, in which the amount of changes in the difference has distinctive distribution characteristics in two orthogonal directions in the sample plane and can vary with the defect morphology. That is to say, the defect as a perturbation would alter the original form birefringence behavior of the nanostructure asymmetrically. More specifically, our method uses the differential signal calculated by subtracting the differential signal of aerial images under X-polarization illumination from that under Y-polarization illumination. The resultant differential image's first-order and second-order transverse gradients have advantages similar to the DPM-based and OPEM-based methods in signal-to-noise ratio (SNR) enhancement [34, 39]. Most importantly, our method is built upon the bright-field microscope, which inherits typical intrinsic merits such as high speed and non-destruction. Both theoretical and experimental investigations for multiple patterned defects via white-light polarization microscopy have been carried out to demonstrate the feasibility and effectiveness of the proposed method established on form-birefringence-breaking imaging. Also, the review results reported by high-resolution SEM have validated the observations using the proposed method. Then, an intelligent classification algorithm for typical patterned defects based on a dual-channel AlexNet neural network has been proposed, stabilizing the classification accuracy of λ/16-sized defects with highly similar features at more than 90%. The strong classification capability of the two-channel network on typical patterned defects can be attributed to the high-order difference image and its transverse gradient being used as the network's input, which highlights the polarization modulation difference between different defects in patterned wafer more significantly than conventional bright-field microscopy results. The proposed method can be seamlessly applied to any other shorter wavelength ranges, including deep-, vacuum- and extreme-ultraviolet, since form birefringence is independent of wavelength. Because the inspection of nanoscale perturbations from the background is widely seen in many other fields, such as distinguishing the pathological changes in tissue cells, detecting abnormal drugs in medicine, identifying the virus or protein molecules, and probing the imperfections in the photomasks and wafers, we believe the method may have a broader impact in diverse areas such as nanoscience, bio-sensing, bio-imaging, semiconductor and so on.

2. Method

2.1. Form-birefringence-breaking-based method for defect inspection

Figure 1 has been used to clarify the principle of the proposed form-birefringence-breaking imaging. Both the asymmetric arrangement of the subwavelength nanostructure along the X- and Y-directions and the geometric asymmetry of the monomer in the nanostructure will cause the dependence of their scattering behavior on the illumination beam polarization. This phenomenon is the so-called form birefringence effect, which has been found and applied in various grating and nanowire arrays [43–45]. As shown in figure 1(a), the near-field intensity difference map [$I_X{}^{\mathrm{def}}$–$I_Y{}^{\mathrm{def}}$] can be determined by subtracting the near-field intensity of the particle-contained nanowire dimer under X-polarization illumination (corresponding to figure 1(b)) from that under Y-polarization illumination (corresponding to figure 1(c)). It can be easily noticed that there are two highly localized intensity peaks around the particle due to the form birefringence effect and the near-field coupling effect. Figures 1(b) and (c) also present noticeable differences in near-field response under the two orthogonal polarization illuminations. Compared with the near-field intensity difference shown in figure 1(a), the localized peaks in the near-field intensity difference [$I_X{}^{\mathrm{back}}$–$I_Y{}^{\mathrm{back}}$] of the defect-free nanowire dimer shown in figure 1(d) are significantly different from those for the particle-contained dimer in terms of both profile and amplitude. Correspondingly, the near-field

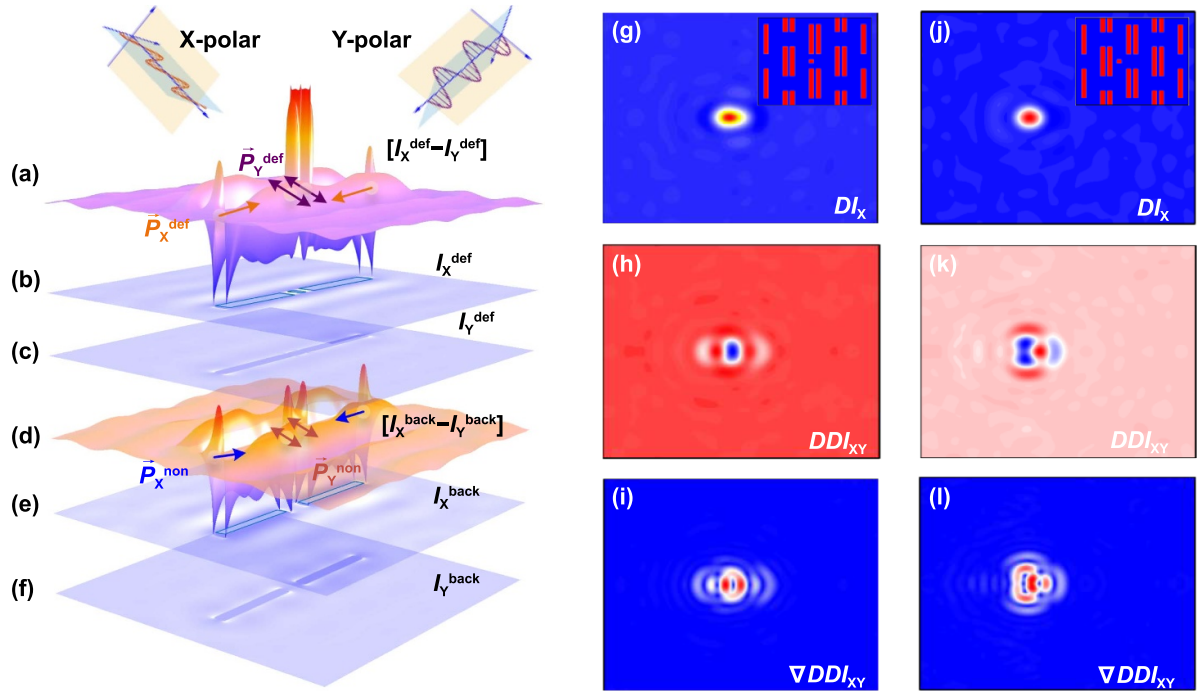

Figure 1. Schematic illuminations of the proposed method: capturing the form-birefringence scattering signal of the defect with the help of switching the polarization of illumination beams. (a) The near-field intensity difference under X- and Y-polarization illuminations, (b) and (c) near-field intensity maps under X-polarization and Y-polarization illuminations for a nanowire dimer with a particle defect located in the center of the dimer. (d) The near-field intensity difference under X- and Y-polarization illuminations, (e) and (f) near-field intensity maps under X-polarization and Y-polarization illuminations for an ideal nanowire dimer. (g)–(i) Far-field intensity difference for periodic arrays of nanowire dimers with and without a particle defect under X-polarization illumination, the differential of far-field intensity difference under X- and Y-polarization illuminations, and its first-order transverse gradient. (j)–(l) Similar results for periodic arrays of nanowire dimers when the particle position shifts. The inset image shown in (g) and (j) exhibits particle positions in the nanowire dimer arrays.

intensity maps of the defect-free nanowire dimer shown in figures 1(e) and (f) are also different from those shown in figures 1(b) and (c), which imply the perturbation caused by the particle in the near field of the dimer under two orthogonal polarization illuminations. Through further calculating the difference between the near-field intensity difference maps shown in figures 1(a) and (d), the resultant nontrivial values would indicate the asymmetry of the perturbation under the two illuminations.

Further, the particle-contained dimer can be extended to the periodic array of nanowire dimers, like the nanostructures shown in the inset images in figures 1(g) and (j). The differences between the dimer arrays mainly lie in the location of the particles. The particles are located in the end-to-end and side-to-side gaps of the adjacent nanowire dimers, respectively. Then, we can evaluate the far-field projection of the near-field intensity perturbation caused by the defect under X-polarization illumination, as shown in figures 1(g) and (j), as well as the difference between the far-field projection results under two orthogonal polarization illuminations, as shown in figures 1(h) and (k). Herein, the resultant high-order differences shown in figures 1(h) and (k) are significantly distinct, while the far-field projection of the near-field intensity perturbation under the X-polarization illumination shown in figures 1(g) and (j) is similar between each other. With the introduction of transverse gradient operation, the first-order gradient maps of the high-order differences for the two particle-contained dimer arrays present apparent differences, as shown in figures 1(i) and (l). The relative position of the particles and the dimer array, namely, the defect morphology formed by the particles and proximity dimers, will determine the asymmetry of the near-field intensity perturbation and its far-field projection under the two orthogonal polarization illuminations. That is to say, the form birefringence in both the near-field perturbation and its far-field projection serves as the theoretical basis for sensing the defect features in patterned wafers via bright-field microscopy combined with the anisotropic polarization illuminations.

The more detailed physical mechanism of the form birefringence-breaking-based defect inspection can be presented below. In the defect-contained nanostructures, such as the particle-contained periodic dimer arrays shown in the inset images in figures 1(g) and (j), the feature size of defects is usually the same as or less than the critical dimension of the nanostructure. Thus, the defect-contained nanostructure can be approximated as the superposition of a square particle and the ideal nanostructure, as shown in figure S1 in the supplementary material. For example, the particle-contained nanowire dimer shown in figure 1(b) can be approximated as the superposition of a square particle in the end-to-end gap and an ideal dimer shown in figure 1(f). According to the electrostatic approximation and the Rayleigh scattering theory

[46, 47], the responses of sub-wavelength particles to the orthogonal polarization illuminations are the same, which does not exhibit the form birefringence feature. Thus, the difference between the results shown in figures 1(a) and (d) can be attributed to the polarization interaction imposed on the particle by the scattering field of the nanowire dimer. More importantly, the magnitude of the polarization interaction depends not only on the polarization state of the scattering field of the nanowire dimer [47], but also on the location relationship between the particle and the nanowire dimer [48]. The former factor can be used as the inspection method, in which the orthogonally polarized light can be illuminated on the sample detected, and the corresponding scattering fields under each polarization can be collected. While the latter can be used as the basis for sensing the defect morphology, because the aforementioned location relationship contains the particle defect's position, orientation, area symmetry, and proximity relative to the nanowire dimer [49]. Various defects, such as bridging, cutting-line, and particles in patterned wafers, can be viewed as the perturbation of specific particles on the ideal nanostructure, but the position relations between them and the background nanostructure are quite different. And the pure scattering field $\mathbf{E}^{\mathrm{part}}(\mathbf{r})$ of the defect varied with the defect type can be approximately evaluated by the Green function method [50],

$$\begin{aligned}\mathbf{E}^{\mathrm{part}}(\mathbf{r}) &= \mathbf{E}^{\mathrm{def}}(\mathbf{r}) - \mathbf{E}^{\mathrm{back}}(\mathbf{r}) \approx \int_{\Omega} G(\mathbf{r}-\mathbf{r}') \\ &\quad \times \chi(\mathbf{r}') \left[\mathbf{E}^{\mathrm{back}}(\mathbf{r}') + \mathbf{E}^{\mathrm{inc}}(\mathbf{r}')\right] \mathrm{d}\mathbf{r}' = \mathbf{E}^{\mathrm{indirect}}(\mathbf{r}) + \mathbf{E}^{\mathrm{direct}}(\mathbf{r}) \\ &= \int_{\Omega} G(\mathbf{r}-\mathbf{r}')\chi(\mathbf{r}')\mathbf{E}^{\mathrm{back}}(\mathbf{r}')\,\mathrm{d}\mathbf{r}' + \int_{\Omega} G(\mathbf{r}-\mathbf{r}') \\ &\quad \times \chi(\mathbf{r}')\mathbf{E}^{\mathrm{inc}}(\mathbf{r}')\,\mathrm{d}\mathbf{r}' \end{aligned} \tag{1}$$

where the Green function $G(\mathbf{r}–\mathbf{r}')$ is the solution of the inhomogeneous Helmholtz equation of the element impulse, which is independent of the polarization state of the excitation field. The scattering potential $\chi(\mathbf{r})$ of the subwavelength particle is also independent of the polarization state of the excitation field, if the subwavelength particle has an in-plane rotational symmetry of order 4 [51]. The total scattering field of the defect-contained dimer array satisfies the relationship $\mathbf{E}^{\mathrm{def}} = \mathbf{E}^{\mathrm{part}} + \mathbf{E}^{\mathrm{back}}$ for all the polarization illuminations. $\mathbf{E}^{\mathrm{def}}(\mathbf{r})$ and $\mathbf{E}^{\mathrm{back}}(\mathbf{r})$ are the scattering fields of the defect-contained and defect-free nanostructure, respectively. Therefore, switching the polarization state of the incident field $\mathbf{E}^{\mathrm{inc}}(\mathbf{r}')$ cannot lead to the amplitude change of the direct component $\mathbf{E}^{\mathrm{direct}}(\mathbf{r})$ in the scattering field $\mathbf{E}^{\mathrm{part}}(\mathbf{r})$. Then, only the significant difference in the background scattering field $\mathbf{E}^{\mathrm{back}}(\mathbf{r})$ under two orthogonal polarization illuminations, caused by the form birefringence of the background nanostructure, will be transferred to the indirect component $\mathbf{E}^{\mathrm{indirect}}(\mathbf{r})$ in the scattered field $\mathbf{E}^{\mathrm{part}}(\mathbf{r})$ of the particle. Meanwhile, the convolution operation in equation (1) enables constructing the correlation between the scattering field $\mathbf{E}^{\mathrm{part}}(\mathbf{r})$ and the defect morphology. When using an imaging objective lens, the low spatial-frequency components of the near-field intensity difference I_{X}–I_{Y} under the two orthogonal polarization illuminations can be transmitted to the imaging plane in the far field. Figure 1(g) or figure 1(j) shows the far-field intensity difference DI_{X} of a particle defect in the periodic array of nanowire dimer, reported by conventional bright-field microscopy under X-polarization illumination, which is almost a circular Airy disk. While figure 1(h) or figure 1(k) shows the far-field intensity difference DDI_{XY} under the two orthogonal polarization illuminations, which is the so-called form-birefringence-breaking image

$$\begin{aligned} DDI_{\mathrm{XY}} &= DI_{\mathrm{X}} - DI_{\mathrm{Y}} = \left[I^{\mathrm{defect}} - I^{\mathrm{back}}\right]_{\mathrm{X}} - \left[I^{\mathrm{defect}} - I^{\mathrm{back}}\right]_{\mathrm{Y}} \\ &= [I_{\mathrm{X}} - I_{\mathrm{Y}}]^{\mathrm{defect}} - [I_{\mathrm{X}} - I_{\mathrm{Y}}]^{\mathrm{back}} = \left[\left|\mathbf{E}_{\mathrm{X}}{}^{\mathrm{part}}\right|^2 - \left|\mathbf{E}_{\mathrm{Y}}{}^{\mathrm{part}}\right|^2\right] \\ &\quad + \left[2\left|\mathbf{E}_{\mathrm{X}}{}^{\mathrm{part}}\right|\left|\mathbf{E}_{\mathrm{X}}{}^{\mathrm{back}}\right|\cos(\Delta_{\mathrm{X}}) - 2\left|\mathbf{E}_{\mathrm{Y}}{}^{\mathrm{part}}\right|\left|\mathbf{E}_{\mathrm{Y}}{}^{\mathrm{back}}\right|\cos(\Delta_{\mathrm{Y}})\right] \end{aligned} \tag{2}$$

where $[I_{\mathrm{X}}–I_{\mathrm{Y}}]^{\mathrm{defect}}$ and $[I_{\mathrm{X}}–I_{\mathrm{Y}}]^{\mathrm{non}}$ measure the form-birefringence scattering properties of the nanowire dimer array with and without particle defect, respectively. $\mathbf{E}_{\mathrm{X}}{}^{\mathrm{part}}$ and $\mathbf{E}_{\mathrm{Y}}{}^{\mathrm{part}}$ are the scattering fields of particles under X- and Y-polarization illuminations, respectively. $\mathbf{E}_{\mathrm{X}}{}^{\mathrm{back}}$ and $\mathbf{E}_{\mathrm{Y}}{}^{\mathrm{back}}$ are the scattering fields of defect-free nanostructure under X- and Y-polarization illuminations, respectively.

With the particle defect perturbing the nanostructure array, both the translational symmetry and the mirror symmetry of the dimer array will be broken, which leads to non-Airy disk-like scattering signal maps shown in figures 1(h) and (k). As shown in figures 1(i) and (l), the first-order transverse gradient of the intensity difference DDI_{XY} highlights the form-birefringence breaking effect caused by the defect, due to the non-homogeneous spatial distribution of the scattering field $\mathbf{E}^{\mathrm{part}}(\mathbf{r})$. It also implies that defects usually disturb the original form-birefringence scattering behavior of the dimer array in an unequal manner. Furthermore, with the change of defect type, the far-field intensity difference map DDI_{XY} will exhibit conspicuous diversity, similar to that between the near-field intensity difference maps shown in figures 1(a) and (d), which can be attributed to the diversity in the perturbation manner and the position relationship. That's the basis for the defect classification or the visualizable detection of sub-wavelength nano-objects by the proposed method. Moreover, with the help of the definition in equation 2, both conventional bright-field inspection tools and the Die-to-Die inspection algorithm can still be invoked [52], which indicates that the proposed method can inherit the advantages of the conventional method, such as the high efficiency and the non-destructiveness. And the second-order differential operation in equation 2 can greatly eliminate the direct contribution from the background scattering field $\mathbf{E}^{\mathrm{back}}$, which enables the reliable discrimination of the defect intrinsic signals.

Considering the orthogonality and completeness of real eigenmodes and eigenvalue sets in module expansion theory, equation (2) can be simplified when the electric fields involved

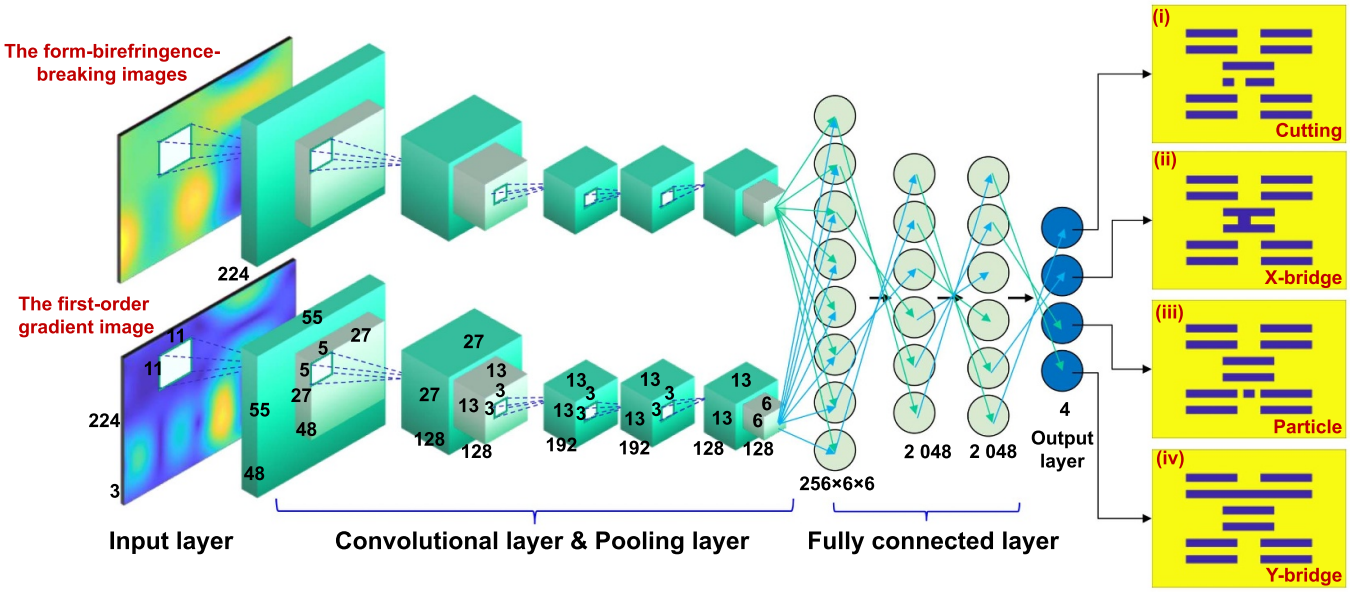

Figure 2. Schematic diagram of the dual-channel AlexNet network structure used in the defect intelligent classification algorithm.

in the above cross terms are located in the same phase and region,

$$\begin{aligned} DDI_{\mathrm{XY}} = & \left[\left|\int_{\Omega} G(\mathbf{r}-\mathbf{r}')\chi(\mathbf{r}')\left[\mathbf{E}_{\mathrm{X}}{}^{\mathrm{back}}(\mathbf{r}')\right]\mathrm{d}\mathbf{r}'\right|^2\right. \\ & \left.-\left|\int_{\Omega} G(\mathbf{r}-\mathbf{r}')\chi(\mathbf{r}')\left[\mathbf{E}_{\mathrm{Y}}{}^{\mathrm{back}}(\mathbf{r}')\right]\mathrm{d}\mathbf{r}'\right|^2\right] \\ & +2\left|\int_{\Omega} G(\mathbf{r}-\mathbf{r}')\chi(\mathbf{r}')\left[\left|\mathbf{E}_{\mathrm{X}}{}^{\mathrm{back}}(\mathbf{r}')\right|^2\right]\mathrm{d}\mathbf{r}'\right| \\ & -2\left|\int_{\Omega} G(\mathbf{r}-\mathbf{r}')\chi(\mathbf{r}')\left[\left|\mathbf{E}_{\mathrm{Y}}{}^{\mathrm{back}}(\mathbf{r}')\right|^2\right]\mathrm{d}\mathbf{r}'\right| \\ \approx & \int_{\Omega} |G(\mathbf{r}-\mathbf{r}')\cdot\chi(\mathbf{r}')+2|\times|G(\mathbf{r}-\mathbf{r}')\cdot\chi(\mathbf{r}')| \\ & \times\left[\left|\mathbf{E}_{\mathrm{X}}{}^{\mathrm{back}}(\mathbf{r}')\right|^2-\left|\mathbf{E}_{\mathrm{Y}}{}^{\mathrm{back}}(\mathbf{r}')\right|^2\right]\mathrm{d}\mathbf{r}'. \end{aligned} \tag{3}$$

Due to the form-order birefringence scattering properties of ideal defect-free nanostructures, the integrand component $|\mathbf{E}_{\mathrm{X}}{}^{\mathrm{back}}(\mathbf{r}')|^2-|\mathbf{E}_{\mathrm{Y}}{}^{\mathrm{back}}(\mathbf{r}')|^2$ in equation (3) will be non-zero, so DDI_{XY} is also non-zero. It can be noted that DDI_{XY} is a scalar function of the position vector $\mathbf{r}$, so DDI_{XY} will have two-dimensional spatial distribution characteristics, which will be the fundamental reason why different types of wafer defects display different patterns of form-order birefringence scattering perturbations. It can be noted that when the defect type changes, the first-order difference DI_{XY} of the scattering intensity of each sample will change significantly, and the second-order difference DDI_{XY} of the scattering intensity will also change significantly. That's the theoretical basis for us to carry out defect feature screening.

2.2. Dual-channel AlexNet neural network-based algorithm for defect classification

An intelligent classification algorithm for typical patterned defects based on a dual-channel AlexNet neural network has been built, in which the second-order differential aerial image DDI_{XY} and its first-order transverse gradient image are the input. The dual-channel AlexNet network convolves and pools these two images and combines them in the fully connected layer to achieve defect feature classification. The specific dual-channel AlexNet network structure used is shown in figure 2. Notably, the definitions of particle and cut defect used in figure 2 conform to the commonly used terminology, whereas the X-bridge and Y-bridge defect types are defined as bridging along the short- and long-period directions, respectively.

The reason for using AlexNet convolutional neural network (CNN) as the central part of the intelligent classification algorithm of defect features comes from the following two aspects [53]. First, the original AlexNet has excellent image classification accuracy and efficiency. It once stood out in the ILSVRC-2012 competition with its ability to accurately classify 1.2 million high-resolution images into 1000 categories. Second, the classification scenario of defect features is consistent with the application scope of the AlexNet network. The input of defect feature classification is usually a vast image database, requiring accuracy and efficiency. In the dual-channel AlexNet CNN shown in figure 2, it includes one input layer, five convolutional layers (C1, C2, C3, C4, C5), and three fully connected layers (FC6, FC7, FC8), and one output layer [54]. In the proposed algorithm, the second-order difference DDI_{XY} of the far-field aerial image and its first-order transverse gradient image are both cropped into an input image of 224 × 224 × 3, where 224 × 224 represents the number of pixels in the orthogonal directions, and 3 represents RGB Number of channels. Using the self-developed rigid vector imaging model introduced in the next section,

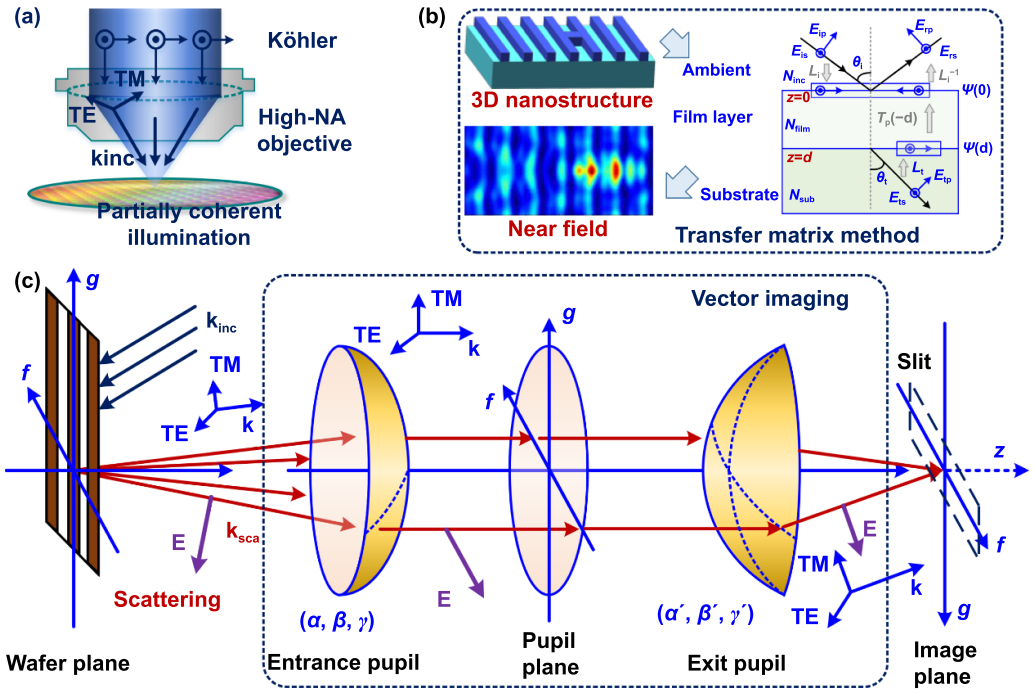

Figure 3. Schematic diagram of the vector diffraction imaging model for high-NA polarization microscopy. (a) Köhler illumination configuration used in the imaging model. (b) Near-field calculation based on Transfer matrix method. (c) Vector diffraction imaging module.

10 800 images can be produced and used as the input training set to train the AlexNet network thoroughly. In the convolutional layer C1, the input image will successfully undergo convolution, rectified linear unit (ReLU), local response normalization (LRN), pooling, and other processing, which will be transformed into a 55 × 55 × 48 image. The convolution process involves using 48 convolution kernels with the size of 11 × 11 × 3 to perform a convolution operation on the input image, in which the edge filling parameter is set to 2, and the movement stride parameter of the convolution kernel is set to 4. This algorithm uses the ReLU function as the activation function of the neuron, due to the high convergence speed. In the C2 convolution layer, the operations, including convolution, ReLU, LRN, and Pooling, are still implemented, except that this layer uses 128 5 × 5 × 48 convolution kernels, the edge filling parameter of 2, and the movement stride parameter of convolution kernel of 1. In the C3 convolutional layer, only the operations, including convolution and ReLU, are implemented. In the C4 convolution layer, only the operations consisting of convolution and ReLU are implemented, while the operations consisting of convolution, ReLU, and Pooling are implemented in the C5 convolution layer. The fully connected layer FC6 is to flatten the image data of the two channels to combine into new data, thereby forming 6 × 6 × 256 matrix data. Subsequently, the operations consisting of neuron deactivation (Dropout), full connection, and ReLU are implemented in the fully connected layers FC6 and FC7, which use 2048 neurons for full connection. Then, ReLU activation is implemented and connected to the fully connected layer FC8 to output the defect type.

2.3. Rigid vector imaging modelling

Figure 3 shows the basic theoretical framework of the self-developed vector imaging simulation tool. In the simulation tool, the imaging process was divided into four parts, namely (a) decomposition of an illumination light field into a series of plane wave components with distinct wave vectors according to the Köhler illumination configuration [55], (b) calculation of the scattering near field for the defect-contained nanostructure based on the Transfer matrix method (TMM) [56], (c) calculation of the electric fields in the entrance pupil plane, the pupil plane, the exit pupil plane and the imaging plane by using the angular spectrum method combined with the vector nature of the electric field [57], (d) calculation of the total imaging based on the Abbe theory [58]. In the Köhler illumination configuration, the input electric field distribution (E_X, E_Y, E_Z) defined in the illumination pupil plane, consists of plane waves with different direction cosines (α_s, β_s, γ_s). Then, they can be transformed into the polarization vector ($E_\perp$, $E_\parallel$), which will be tracked throughout the optical system for modelling the imaging process.

$$\begin{bmatrix} E_\perp(\alpha_s,\beta_s) \\ E_\parallel(\alpha_s,\beta_s) \end{bmatrix} = \frac{1}{\gamma_s}\begin{bmatrix} -\beta_s\gamma_s/\rho_s & \alpha_s\gamma_s/\rho_s \\ -\alpha_s/\rho_s & -\beta_s/\rho_s \end{bmatrix}\begin{bmatrix} E_X(\alpha_s,\beta_s) \\ E_Y(\alpha_s,\beta_s) \end{bmatrix} \tag{4}$$

where $\rho_s = \mathrm{sqrt}\,(\alpha_s{}^2 + \beta_s{}^2)$. In the spatial frequency domain, the polarization vector ($E_\perp$, $E_\parallel$) is orthogonal with the wave vector $\mathbf{k}_{inc}$ of the corresponding plane wave component. By assuming that each plane wave component is illuminating

the nanostructure uniformly, the scattering near field from the nanostructure can be calculated by approximately solving Maxwell's equations based on TMM. Since the structure defect breaks the period of the nanostructure, the supercell-based Bloch-period boundaries are utilized to isolate the near-field coupling between the defects [59]. The scattering near field calculated by TMM is usually the field distribution in the spatial Cartesian coordinate system, which consists of three field components such as $E_X(x,\ y,\ 0)$, $E_Y(x,\ y,\ 0)$, and $E_X(x,\ y,\ 0)$ with $z = 0$ representing the sample plane. By assuming that the near field is obtained by coherently summing all the plane wave components, the plane wave angular spectrum can be calculated using the Fourier transformation [57]

$$E_X(f_x,f_y,0) = \int\int_{+\infty}^{+\infty} E_X(x,y,0)\exp\left[-j2\pi\left(f_X x + f_Y y\right)\right]\mathrm{d}x\mathrm{d}y \tag{5a}$$

$$E_Y(f_x,f_y,0) = \int\int_{+\infty}^{+\infty} E_Y(x,y,0)\exp\left[-j2\pi\left(f_X x + f_Y y\right)\right]\mathrm{d}x\mathrm{d}y. \tag{5b}$$

Considering the transverse wave nature of the electromagnetic waves, only E_X and E_Y need to be calculated at the entrance pupil, imaging pupil plane, and exit pupil, and E_Z will be determined by E_X and E_Y. Since the bright field inspection microscopy is the object-space telecentric system, the entrance pupil can be considered to be at infinity. Correspondingly, the electric field E_X and E_Y in the entrance pupil can be still calculated by using the angular spectrum method,

$$\begin{aligned} E_X(f_Y,f_Y,z) &= E_X(f_X,f_Y,0)\exp\left[j\frac{2\pi z}{\lambda}\sqrt{1-(\lambda f_X)^2-(\lambda f_Y)^2}\right] \\ &\approx E_X(f_X,f_Y,0) \end{aligned} \tag{6a}$$

$$\begin{aligned} E_Y(f_X,f_Y,z) &= E_Y(f_X,f_Y,0)\exp\left[j\frac{2\pi z}{\lambda}\sqrt{1-(\lambda f_X)^2-(\lambda f_Y)^2}\right] \\ &\approx E_Y(f_X,f_Y,0) \end{aligned} \tag{6b}$$

where the exponential term will be approximated as a constant independent of the spatial frequency f_X and f_Y. Thus, the electric field in the entrance pupil will be approximated as the angular spectrum of the near field. Considering the Fourier frequency-shift effect caused by the direction cosines of the plane wave in the illumination pupil, the electric field in the entrance pupil needs to be corrected,

$$\begin{aligned} E_X(\alpha_{ent},\beta_{ent},\infty) = {} & E_X(\lambda f_X,\lambda f_Y,0) \\ & \cdot Circ\left(\frac{\sqrt{(\lambda f_X-\alpha_s)^2+(\lambda f_Y-\beta_s)^2}}{NA}\right) \\ & \cdot \frac{\sqrt{1-{\alpha_{ent}}^2-{\beta_{ent}}^2}}{\sqrt{1-{\beta_{ent}}^2+|\alpha_{ent}\cdot\beta_{ent}|}} \end{aligned} \tag{7a}$$

$$\begin{aligned} E_Y(\alpha_{ent},\beta_{ent},\infty) = {} & E_Y(\lambda f_X,\lambda f_Y,0) \\ & \cdot Circ\left(\frac{\sqrt{(\lambda f_X-\alpha_s)^2+(\lambda f_Y-\beta_s)^2}}{NA}\right) \\ & \cdot \frac{\sqrt{1-{\alpha_{ent}}^2-{\beta_{ent}}^2}}{\sqrt{1-{\beta_{ent}}^2+|\alpha_{ent}\cdot\beta_{ent}|}} \end{aligned} \tag{7b}$$

where the circular domain function *Circ* has the effect of low-pass filtering. And the third term in the right-hand side of equation (7) is used to compensate for the transverse wave effect. *NA* is the numerical aperture of the objective lens, and λ is the light wavelength. And α_{ent} and β_{ent} are the corrected direction cosine coordinates in the entrance pupil. And they can be expressed as follows,

$$\beta_{ent} = (\lambda f_Y-\beta_s)\cdot Circ\left(\frac{\sqrt{(\lambda f_X-\alpha_s)^2+(\lambda f_Y-\beta_s)^2}}{NA}\right) \tag{8a}$$

$$\alpha_{ent} = (\lambda f_X-\alpha_s)\cdot Circ\left(\frac{\sqrt{(\lambda f_X-\alpha_s)^2+(\lambda f_Y-\beta_s)^2}}{NA}\right). \tag{8b}$$

As for the vector propagation from the entrance pupil to the exit pupil, the polarization aberration, the wave-front aberration, and the obliquity factor need to be fully considered in the propagation model. Meanwhile, the electric field in the entrance pupil needs to be transformed into the polarization vector, which is convenient for calculating the polarization aberration effect using the Jones pupil method

$$\begin{aligned} \begin{bmatrix} E_\perp(\alpha_{ent},\beta_{ent}) \\ E_\parallel(\alpha_{ent},\beta_{ent}) \end{bmatrix} = {} & \frac{1}{\gamma_{ent}}\begin{bmatrix} -\beta_{ent}\gamma_{ent}/\rho_{ent} & \alpha_{ent}\gamma_{ent}/\rho_{ent} \\ -\alpha_{ent}/\rho_{ent} & -\beta_{ent}/\rho_{ent} \end{bmatrix} \\ & \times \begin{bmatrix} E_X(\alpha_{ent},\beta_{ent}) \\ E_Y(\alpha_{ent},\beta_{ent}) \end{bmatrix}. \end{aligned} \tag{9}$$

Then, the electric field in the exit pupil can be calculated by the following equation,

$$\begin{aligned} \begin{bmatrix} E_\perp(\alpha_{ext},\beta_{ext}) \\ E_\parallel(\alpha_{ext},\beta_{ext}) \end{bmatrix} = {} & \sqrt[4]{\frac{1-M^2\cdot\left({\alpha_{ent}}^2+{\beta_{ent}}^2\right)}{1-\left({\alpha_{ent}}^2+{\beta_{ent}}^2\right)}} \\ & \cdot\begin{bmatrix} J_{\perp\perp}\left(\frac{\alpha_{ent}}{NA},\frac{\beta_{ent}}{NA}\right) & J_{\perp\parallel}\left(\frac{\alpha_{ent}}{NA},\frac{\beta_{ent}}{NA}\right) \\ J_{\parallel\perp}\left(\frac{\alpha_{ent}}{NA},\frac{\beta_{ent}}{NA}\right) & J_{\parallel\parallel}\left(\frac{\alpha_{ent}}{NA},\frac{\beta_{ent}}{NA}\right) \end{bmatrix} \\ & \cdot\exp\left[-jk\left(\Delta z\cdot(\gamma_{ent}-1)+\sum_{n=1}^{37}C_n \right.\right. \\ & \left.\left.\cdot R_n\left(\frac{\alpha_{ent}}{NA},\frac{\beta_{ent}}{NA}\right)\right)\right]\cdot\begin{bmatrix} E_\perp(\alpha_{ent},\beta_{ent}) \\ E_\parallel(\alpha_{ent},\beta_{ent}) \end{bmatrix} \end{aligned} \tag{10}$$

where M is the magnification of the objective lens. $J_{\perp\perp}$, $J_{\perp\parallel}$, $J_{\parallel\perp}$, and $J_{\parallel\parallel}$ are the Jones matrix elements of the Jones

pupil. C_n and R_n are the nth Zernike coefficients and Zernike terms, respectively. Δz is the defocus. $\alpha_{\text{ent}} = \alpha_{\text{ent}}/M$ and $\beta_{\text{ent}} = \beta_{\text{ent}}/M$ are the direction cosine coordinates in the exit pupil. The first term in the right-hand side of equation (1) is used to consider the radio-metric correction effect. In order to coherently sum the contributions of each plane wave in the exit pupil to the electric field in the imaging plane, it is necessary to transform the electric field in the exit pupil from the local coordinate system to the global coordinate system

$$\begin{bmatrix} E_{\text{X}}(\alpha_{\text{ext}},\beta_{\text{ext}}) \\ E_{\text{Y}}(\alpha_{\text{ext}},\beta_{\text{ext}}) \\ E_{\text{Z}}(\alpha_{\text{ext}},\beta_{\text{ext}}) \end{bmatrix} = \begin{bmatrix} \frac{-\beta_{ext}}{\sqrt{\alpha_{\text{ext}}{}^2+\beta_{\text{ext}}{}^2}} & \frac{-\alpha_{\text{ext}}\cdot\sqrt{1-\alpha_{\text{ext}}{}^2-\beta_{\text{ext}}{}^2}}{\sqrt{\alpha_{\text{ext}}{}^2+\beta_{\text{ext}}{}^2}} \\ \frac{\alpha_{\text{ext}}}{\sqrt{\alpha_{\text{ext}}{}^2+\beta_{\text{ext}}{}^2}} & \frac{-\beta_{\text{ext}}\cdot\sqrt{1-\alpha_{\text{ext}}{}^2-\beta_{\text{ext}}{}^2}}{\sqrt{\alpha_{\text{ext}}{}^2+\beta_{\text{ext}}{}^2}} \\ 0 & \sqrt{\alpha_{\text{ext}}{}^2+\beta_{\text{ext}}{}^2} \end{bmatrix} \times \begin{bmatrix} E_{\perp}(\alpha_{\text{ext}},\beta_{\text{ext}}) \\ E_{\parallel}(\alpha_{\text{ext}},\beta_{\text{ext}}) \end{bmatrix}. \tag{11}$$

Then, a Fourier inversion transform has been carried out to calculate the total electric field at the imaging plane, which is the result of the interference of different plane waves in the exit pupil

$$\begin{aligned} \text{E}_{\text{ii}}(x',y') = \int\int_{-\infty}^{+\infty} & \text{E}_{\text{ii}}(\alpha_{\text{ext}},\beta_{\text{ext}}) \\ & \times \exp\left[j2\pi\left(\frac{\alpha_{\text{ext}}}{\lambda}x' + \frac{\beta_{\text{ext}}}{\lambda}y'\right)\right] \\ & \cdot \exp\left[-j2\pi\left(\frac{\alpha_{\text{s}}}{\lambda}x' + \frac{\beta_{\text{s}}}{\lambda}y'\right)\right] \text{d}\alpha_{\text{ext}}\text{d}\beta_{\text{ext}} \end{aligned} \tag{12}$$

where ii represents X, Y, or Z. According to the Abbe imaging theory, the final intensity image can be obtained by summing the intensity images produced by each plane wave in the illumination pupil. Considering the intensity map $e(\alpha_{\text{s}}, \beta_{\text{s}})$ in the illumination pupil, the final intensity image can be calculated by the following formula,

$$\begin{aligned} I = \int\int e(\alpha_{\text{s}},\beta_{\text{s}}) \cdot \Big[& |E_{\text{X}}(x',y')|^2 + |E_{\text{Y}}(x',y')|^2 \\ & + |E_{\text{Z}}(x',y')|^2 \Big] \text{d}\alpha_{\text{s}}\text{d}\beta_{\text{s}}. \end{aligned} \tag{13}$$

In order to ensure the simulation efficiency, a sparse sampling of the direction cosine in the illumination pupil has been implemented to reduce the frequency of TMM near-field calculation. Phase correction caused by off-axis illumination is carried out to compensate for the results in the sparse sampling framework. Meanwhile, the frequency spectrum in the entrance pupil has also been compressed to reduce the calculation scale further.

3. Results and discussion

A series of virtual simulation experiments on the defect-contained periodic nanostructure were carried out first to validate the proposed method. All the simulations were implemented by using the self-developed tool for vector Abbe imaging, in which the near field of various samples was calculated by the transfer matrix method [56]. In the unit cell of the nanostructure, each nanowire is 200 nm wide by 1600 nm long by 100 nm tall. The minor gap between two adjacent nanowires is 100 nm, while the larger is 600 nm. The edge-to-edge gap for the nanowires is 800 nm. The horizontal and perpendicular pitches are 2200 nm and 2400 nm, respectively. The particle is 200 nm wide by 200 nm long by 100 nm tall. The widths of both the perpendicular and horizontal bridging defects are 200 nm. Both the nanowire and the substrate are made up of silicon. Critical simulation settings include that the incident light is X- and Y-polarized focused light with a wavelength of 580 nm, the illumination pupil is a circular surface with a partial coherence factor of 1.0, and the imaging objective is a lens with NA of 0.80 and magnification of 100X.

The corresponding results for the periodic nanostructures perturbed by a particle, a Y-bridge defect, and an X-bridge defect are shown in figures 4(a)–(c), respectively, in which the magnitude has been normalized to the intensity of the light source. As shown in figure 4, the first-row maps show the topology of various perturbed nanostructures, and the second-row maps represent the corresponding far-field intensity difference DDI_{XY}. The third- and fourth-row maps exhibit the first- and second-order transverse gradient of the far-field intensity difference, respectively. It can be easily found that all the DDI_{XY} maps are no longer Airy-like patterns but a mirror-symmetrical pattern, which is just like a blue broad bean partially wrapped by a red circular or crescent moon. With the change of defect types, the profiles of both blue and red spots will change, which obviously exhibits the difference in the form-birefringence-breaking properties of each defect. And the position of the red spot in the DDI_{XY} maps corresponds to the opening direction of the local pattern perturbed by the defect. Meanwhile, the alignment axis between the blue and red spots implies the mirror symmetry axis. The magnitudes of both peaks and valleys in the DDI_{XY} maps are significantly different for each defect. These diverse far-field intensity difference maps can be directly used for defect classification based on prior knowledge of the reference layout of the nanostructure. Moreover, using the first- and second-order transverse gradient, both the spatial distribution characteristics and edge features of the DDI_{XY} maps will be sharply identified, enhancing the sensitivity of defect classification.

Meanwhile, the proposed method was also validated by a series of inspection experiments on three defect-contained samples based on self-built polarization microscopy. In the polarization microscopy shown in figure 5(a), the light source is a high-intensity and wide-spectrum white-light source (LDLS EQ77, Energetic Technology), the polarization state generator (PSG) in the illumination light path is composed of a polarizer (PGT5012, Union Optics), a zero-order quarter wave-plate (@633 nm, Union Optics), and a polarizer (PGT5012, Union Optics). The whole illumination light path is realized based on the Köhler illumination scheme. An Olympus plan-apochromat 100X/0.8NA objective lens (LMPlanFL N 100X/0.80 BD, Olympus) is used together with a 4f lens system in the collection light path to ensure the

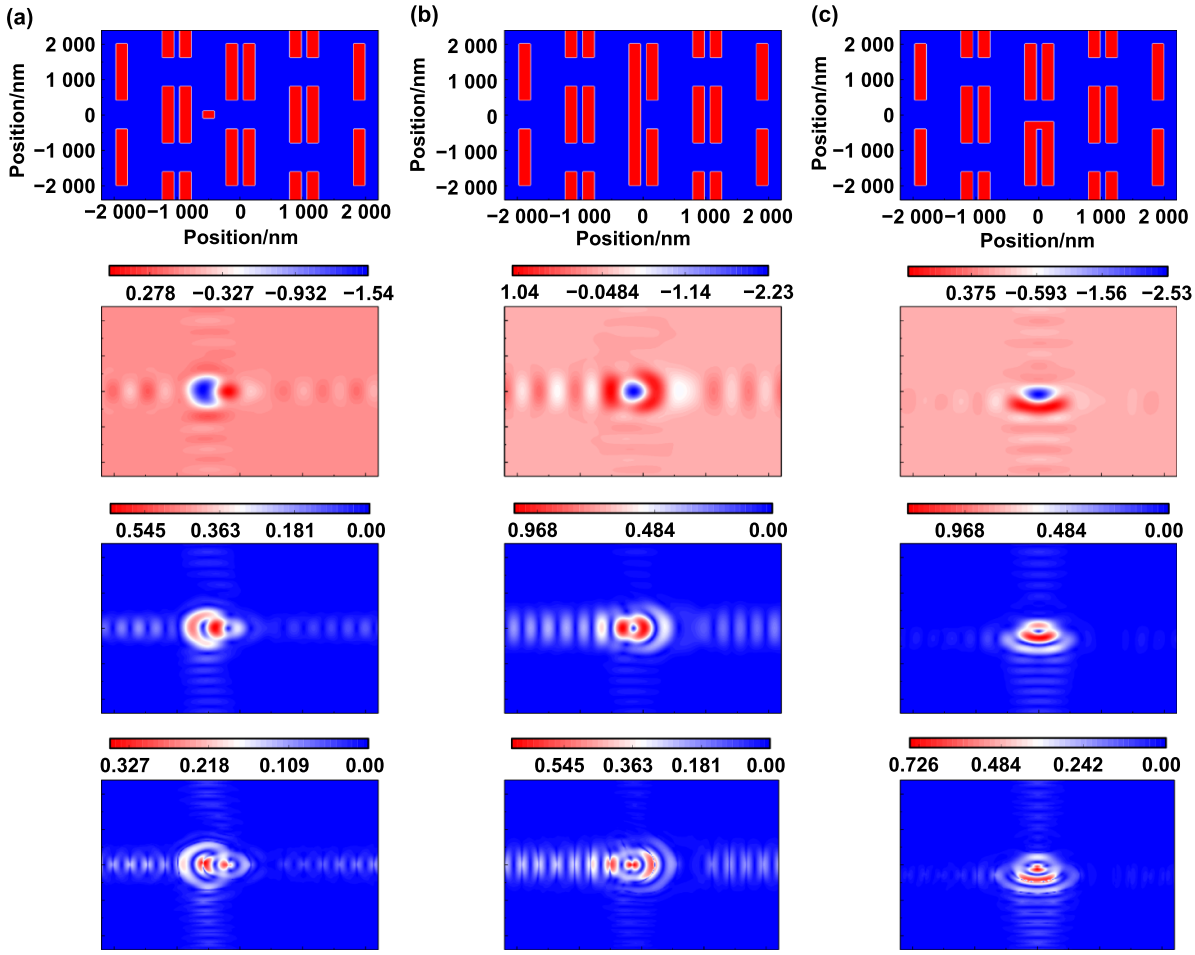

Figure 4. Simulation results of the form birefringence-breaking imaging for the 2D periodic nanostructure perturbed by various defects. (a) The results for the particle defect, (b) for the Y-bridge defect, and (c) for the X-bridge defect. The first-row maps show the topology of the defect-contained nanostructure, and the second-row maps exhibit the far-field intensity difference DDI_{XY} under the two orthogonal polarization illuminations. The third- and fourth-row maps present the first- and second-order transverse gradient of the far-field intensity difference DDI_{XY}, respectively. All the magnitude has been normalized to the intensity of the light source.

optical resolution. A high-resolution CMOS camera (Prosilica GT 1930 with Sony IMX174, Allied Vision) is used to capture the high-definition images of samples. A motorized three-axis stage (PT3 with ZST225B actuators, Thorlabs Inc.) with 10 nm step precision is used to adjust the samples into the depth of focus and to translate the field of view over the sample surface. The defect-contained samples (Customized samples, Monta Vista Inc.) are the same as those in the simulation experiments shown in figure 2. And much more details about the experiment samples and the post-process method can be found in supplementary material.

Before detection, the sample needs to be placed horizontally on the sample stage so that the nanowire dimers in the specimen are parallel to the *x*-axis of the instrument coordinate system. This pre-alignment will facilitate determining the X-polarized and Y-polarized lighting conditions by rotating the second polarizer. Since the self-built polarization microscopy has a low-magnification objective lens, aligning the nanowire dimers with the *x*-axis of the instrument coordination system is easy to manipulate, and we could achieve acceptable pre-alignment in the laboratory using only manual manipulation. This alignment method is compatible with the pre-alignment technology widely used in IC production lines. During the experiment, by continuously changing the azimuth angle of the polarizer with a step of 3°, a series of aerial images were collected by the CMOS camera, in which the brightest and darkest aerial images could be used to determine the incident light with the polarization parallel and perpendicular to the nanowires in the samples. The pre-alignment accuracy requirements in previous experiments were not strict because nearly orthogonal or orthogonal X- and Y-polarized illuminations were sufficient to obtain defect-contained samples' asymmetric form birefringence response. It should be emphasized that when using a polarizer to switch the illumination polarization state, the defective sample is always stationary, making it possible to minimize misalignment noise in the differential calculation. That is to say, for existing bright field detection equipment in the industry, orthogonally polarized illuminations can be achieved by simply introducing a polarization modulation method based on rotating polarizers, liquid crystal variable retarders, or photo-elastic modulators. In particular, these illumination polarization modulation technologies are pretty

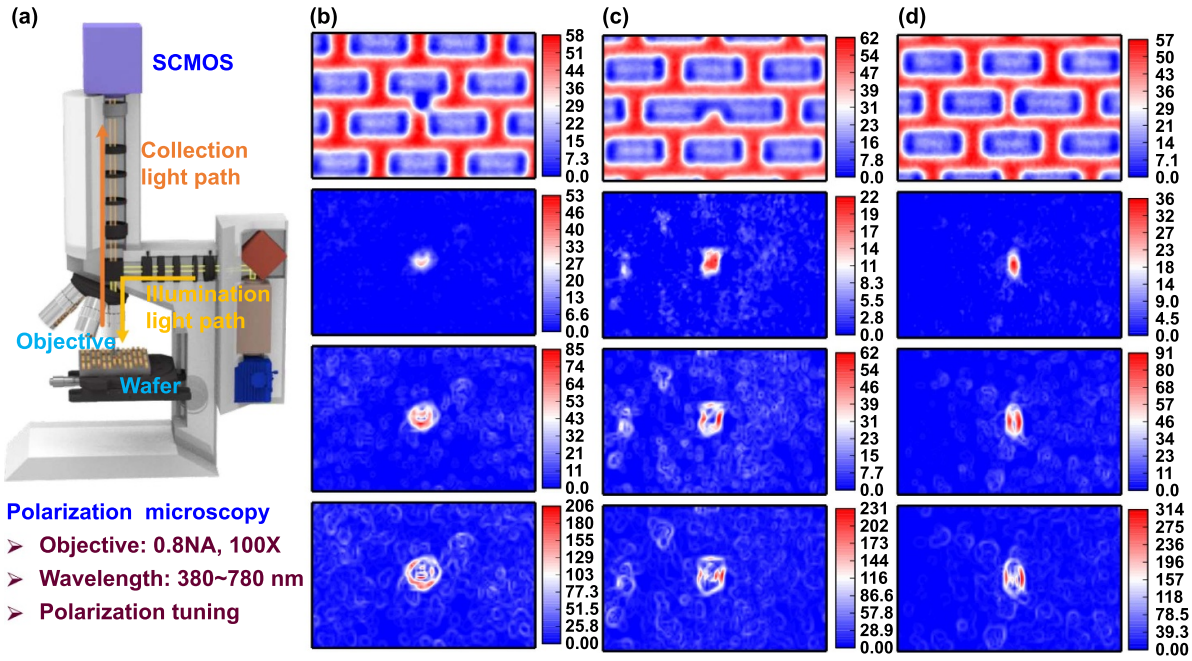

Figure 5. Experimental results for the form birefringence-breaking-imaging-based inspection of the defect-contained periodic nanostructures. (a) The schematic diagram of the self-built polarization microscopy. (b) The results for the particle defect, (c) for the Y-bridge defect, and (d) for the X-bridge defect. The first-row maps show the aerial images of the defective areas in the nanostructure, and the second-row maps exhibit far-field intensity difference DDI_{XY} under the two orthogonal polarization illuminations. While the third- and fourth-row maps present the first- and second-order transverse gradients of the DDI_{XY}, respectively. All the aerial images reported by polarization microscopy are high-resolution images, which can reveal the defect types. The geometric dimensions of these samples are the same as those of the simulated object in figure 4. All the resulting maps are in units of grayscale values from 0 to 255.

mature and have extremely short modulation times, so it is predicted that they will not cause a substantial reduction in defect detection yield.

Then, several sets of aerial images were captured under the two orthogonally polarized illuminations. Since the feature sizes of both nanostructure and defects on the samples were in the order of 200 nm, quite close to the Abbe–Rayleigh diffraction limit of the microscopy [60], the defect-contained nanostructure could be imaged by the microscopy. The imaging results under the X-polarization illumination are shown in the first-row maps in figures 5(b)–(d). These aerial images have been calibrated based on the non-uniform background intensity correction algorithm and the tilting distortion correction algorithms [61]. Although the precise edges of an individual nanowire or defect cannot be resolved, it is possible to discern the rough contour of both the particle and the nanowire dimer. The Y-bridge defect can be captured by identifying the nanowire dimer with an anomalous length, while the X-bridge defect can be captured by identifying two nanowire dimers with an anomalous end-to-end gap. By using the Die-to-Die inspection algorithm, the far-field intensity difference DDI_{XY} under the two orthogonal polarization illuminations can be determined, as shown in the second-row maps in figures 5(b)–(d). It can be easily found that the DDI_{XY} maps for each defect are significantly different from each other, not only in profile but also in magnitude. And the grayscale difference between the red and blue spots is at least larger than 20, which reveals the form-birefringence-breaking effect rather than the experimental errors. As shown in the third and fourth rows in figure 5, the first- and second-order transverse gradient of the DDI_{XY} maps further enhances the diversity in the form birefringence-breaking effect. Meanwhile, the experimental results in figure 5 are similar to the simulation results in figure 4, especially in orientation, symmetry, and contour. According to these experimental observations, the form-birefringence-breaking images combined with their transverse gradient will vary strikingly with the change of defect types, which enables the realization of the defect classification based on the proposed method. Moreover, the aerial images in the first row can confirm the accuracy of the correspondence between the defect types and the observation results. It is worth noting that the observation results in figure 5 not only confirm the reliability of the proposed method but also confirm the reasonableness of the simulation method.

Besides, there are cloud-like noise speckles in the sub-images of the second row to the fourth row in figure 5, which might be caused by the camera noise, the registration error, the low-frequency jitter of specimen stage, or the random and weak speckle in the illumination source. However, due to the significant difference between cloud-like noise spots and the effective signal distribution, other noise spots, except registration errors, will not affect the identification of defect features. When checking the differential results DI_X, the high-order differential results DDI_{XY}, and their transverse gradient, the increase in the difference operations leads to the increasingly noticeable cloud-like noise speckles. It indicates that

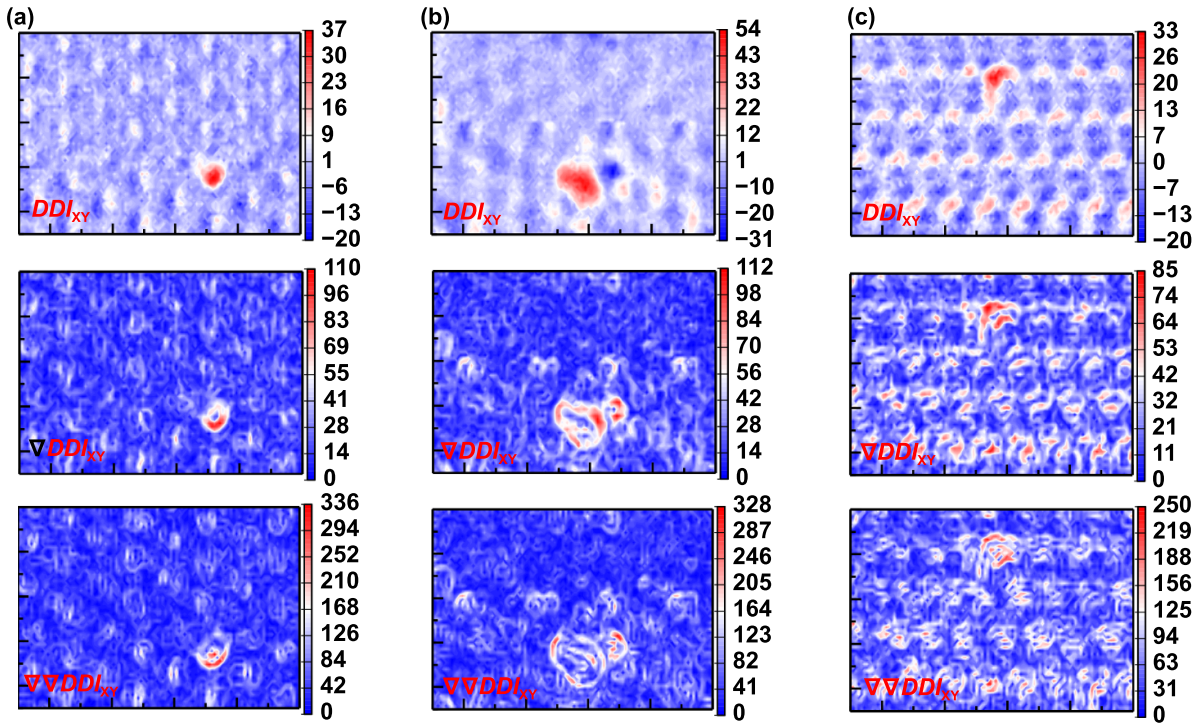

Figure 6. Experimental results for the form birefringence-breaking-imaging-based inspection of the defect-contained periodic nanostructures with a CD of 60 nm. (a) The results for the Y-bridge defect, (b) for the X-bridge defect, and (c) for the cutting-line defect. All these defects have nominal width of 60 nm. The first-row maps exhibit far-field intensity difference DDI_{XY} under the two orthogonal polarization illuminations. While the second- and third-row maps present the first- and second-order transverse gradients of the DDI_{XY}, respectively. The nanowire dimer array has a similar structure as that in figure 5. While the nanowire's length and width are 700 nm and 60 nm, respectively. And the nominal widths of all the defects are 30 nm, 100 nm, and 60 nm. Herein, all the aerial images captured by polarization microscopy can only be used to identify whether the defect exists, and they cannot tell out the defect morphology. All the resulting maps are in units of grayscale values from 0 to 255.

the second-order transverse gradient of DDI_{XY} might not be suitable for classifying defect features. Considering that high-order difference DDI_{XY} requires three consecutive Cell-to-Cell or Die-to-Die algorithms, the registration error between the reference and target images to be detected will have a significant impact on the high-order difference image under the two orthogonal polarization illuminations, namely, minor registration errors will have a noteworthy effect on the accuracy of defect classification. In the newly added experimental results, due to the existence of unshieldable vibration sources in the lab environment, the sample stage is constantly subjected to forced vibrations with small magnitudes, which increases the registration error between reference and target cells, which results in poorer detection results shown in figure 6 than in figure 5. Nevertheless, figure 6 still presents the difference in the form birefringence scattering behaviors between the $\lambda/10$-sized cutting-line and bridging defects (containing Y-bridge and X-bridge defects), indicating the proposed method's capability in capturing anisotropic scattering information helpful for defect classification. Since the system hardware configuration consists of a broadband white light source with a spectrum of 380 nm–780 nm and an objective lens with NA = 0.80, the theoretical imaging-resolution limit is 290 nm, which means the imaging system can capture defects or nanowire dimers with characteristic sizes larger than 290 nm in at least one dimension. In the experiments, the shortest length of a single nanowire in the dimer periodic arrays detected has reached 700 nm, so even cutting-line defects with a width of 60 nm or bridging defects with a width of 30 nm can still be effectively identified using the polarization microscope. The underlying physical mechanism is that all defect features are geometrically composed of the same material or void particles and proximal nanowire dimers, which makes it entirely feasible to identify 30 nm-width defect features in a pattern with a CD of 60 nm. That is why polarization microscopy can still identify the deep sub-wavelength defects despite non-negligible registration errors. Given the highly significant registration error in figure 6, we will further explore more accurate registration algorithms in the future and introduce an active-vibration-isolation table to improve the defect characteristic performance of the proposed method.

Further, the proposed method was applied to the defect-contained nanostructures with small critical dimensions, which would be helpful in evaluating the upper-performance limit of the proposed method. By choosing the deep ultraviolet wavelength at 260 nm, commonly used in the industry for defect inspection, a series of simulations for various defects with sizes ranging from 180 nm to 10 nm were carried out to reveal the adaptability and extensibility of the proposed method. In order to relatively objectively assess the performance of the proposed method in the visualizable detection of defects, the evaluation of defect detectability and the degree of

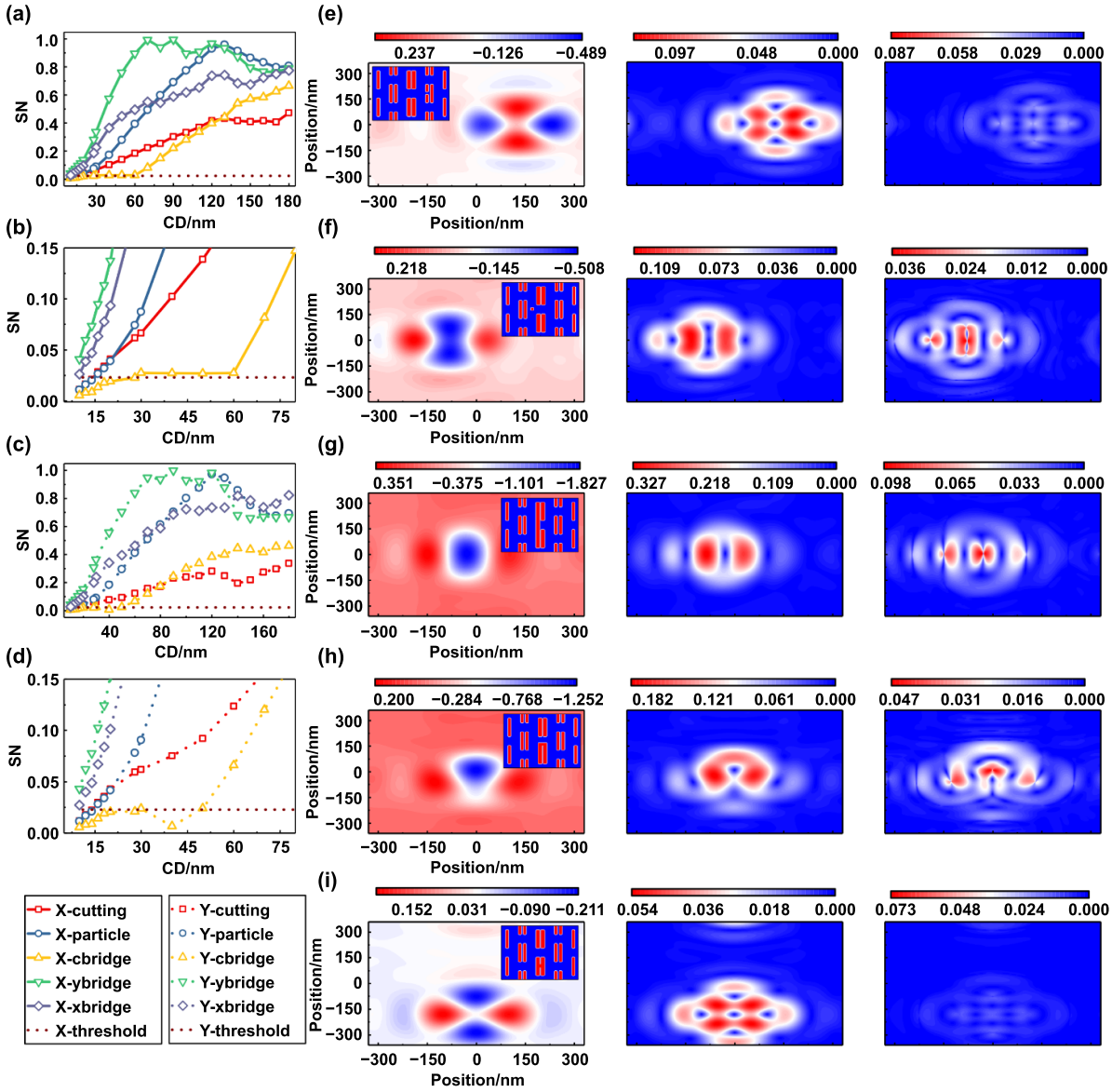

Figure 7. Simulation results of the form birefringence-breaking imaging for various defects at wavelength of 260 nm. From (a) to (d), the simulated inspection sensitivity curves for five defects are shown, in which two orthogonal polarization illuminations have been used. The feature size of the defect is scaled synchronously with the critical dimension of the nanowire. From (e) to (i), the simulation results of the form-birefringence-breaking images for various defects with a feature size of 30 nm are presented. The second-column maps are the far-field intensity difference DDI_{XY}, while the third- and fourth-columns exhibit the first- and second-order transverse gradient maps, respectively. The concerned five defects are the cutting-line defect, the particle defect, the Y-bridge defect, the X-bridge defect, and the central X-bridge defect, respectively. The inset images in the second column show the topology of the defect-contained nanostructure.

intuition of defect classification has been discussed in detail. In comparison with the previously reported rule [10, 62], the detectability criterion has been further improved, as shown below,

$$SN = \frac{\mathrm{Max}\,(DI_{\mathrm{X}})}{\mathrm{Mean}\,(I_{\mathrm{non}})} \geq V_{\mathrm{th}} = k\frac{\sqrt{2}\cdot N_{\mathrm{shot}}}{N_{\mathrm{FWC}}} = 0.023 \qquad (14)$$

where SN is the normalized scattering signal of defect. DI_{X} represents the aerial image difference under the X-polarization illumination, and I_{non} is the aerial image of the defect-free sample under the same illumination. Operators Max and Mean are used to extract the maximum and the mean values, respectively. V_{th} is the threshold for identifying the defects, which was determined using empirical estimation and statistical analysis. In order to ensure the high detection rate and low false alarm rate for defect inspection, the confidence factor k could be initially set to 3. By using the empirical ratio of 0.53% between the shot noise N_{shot} and the full well capacity N_{FWC} in a typical time-delay-integration camera, the threshold V_{th} for identifying defects can be set to 0.023.

Figures 7(a) and (b) together present the sensitivity curves for defect inspection under the X-polarization illumination, while figures 7(c) and (d) together show the sensitivity curves under the Y-polarization illumination. It indicates that the

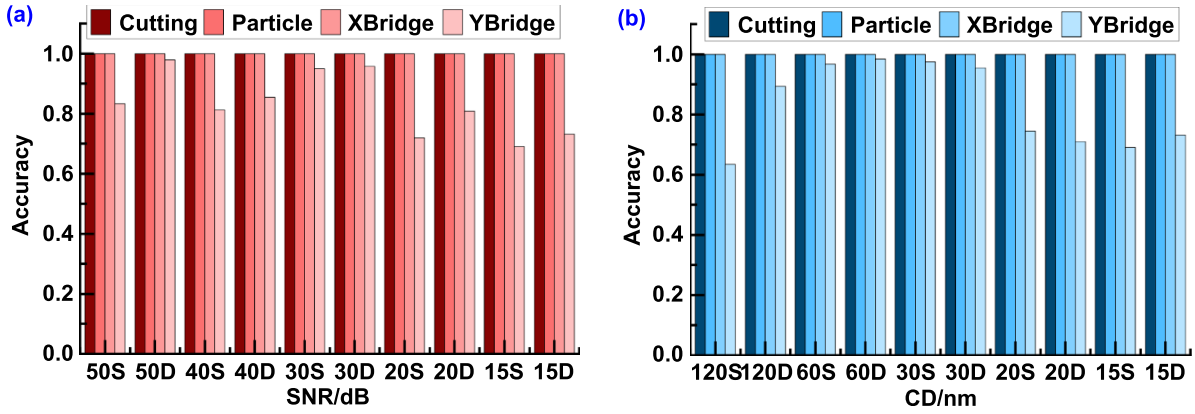

Figure 8. Comparison of noise immunity and classification sensitivity characteristics of single-channel and dual-channel AlexNet networks. (a) The noise immunity characteristics of the single- and dual-channel AlexNet networks, (b) the classification sensitivity characteristics of the single- and dual-channel AlexNet networks.

cutting-line defect, the particle defect, the Y-bridge defect, the X-bridge defect, and the central X-bridge defect with sizes respectively larger than 16 nm, 16 nm, 10 nm, 10 nm, and 30 nm can be detected with reliable signal-to-noise ratio under the two orthogonal polarization illuminations. Then, the simulation results for various defects with a feature size of 30 nm were discussed in figures 7(e)–(i). Figure 7(e), including three sub-figures in the top row, presents the simulation results for the cutting-line defect using the proposed method. Figure 7(f), including three sub-figures in the second row, shows the simulation results for the particle defect, while figure 7(g), including three sub-figures in the third row, presents the simulation results for the Y-bridge defect. Figure 7(h), including three sub-figures in the fourth row, shows the simulation results for the X-bridge defect. Figure 7(i), including three sub-figures in the bottom row, presents the simulation results for the central X-bridge defect. According to the second column in figure 6, the diversity in the DDI_{XY} maps for each defect can be visually identified, due to the difference in the contour, the amplitude, and the symmetry. As for the difference in the pattern profiles between the DDI_{XY} maps in figure 4 and that in figure 7, it might be attributed to the size dependency of the form-birefringence-breaking effect [63]. With the feature size of defects much smaller than the wavelength, more high-order scattering components will carry prominent energy to escape the objective lens's collection range, leading to an inherently weak aerial image in the camera. Thus, the far-field intensity difference DDI_{XY} will be relatively small. The first-order transverse gradient maps shown in the third column of figure 7 still enhance the diversity in the form-birefringence-breaking images for each defect, while the second-order transverse gradient maps displayed in the fourth column of figure 7 have little enlightenment due to the extremely weak magnitude. These results indicate that the form-birefringence-breaking effect caused by the defects with a feature size of 30 nm can be observed by the DDI_{XY} maps and their first-order transverse gradient. In other words, using the proposed method, the deep sub-wavelength defects can be visually sensed by polarization microscopy with the deep ultraviolet wavelength. The simulation work only extends to the 30 nm-sized defects, which is limited by the detectability of the central X-bridge defect. Suppose only the first four defect types are concerned, the proposed method will also be feasible in detecting and classifying defects with feature sizes of 16 nm, i.e. the morphology of defects with sizes of about $\lambda/16$ can be sensed by the proposed method. Through extending the light wavelength to the vacuum- and extreme-ultraviolet spectra, it can be expected that the proposed method will have the potential to visually detect some single-nanometer-scale defects. Given that any nanoscale object or perturbation and its background pattern have the form-birefringence-breaking property, the proposed method can also be used to visually sense these nanoscale objects, such as anomalous biological macro-molecules, viruses, etc.

Figures 8(a) and (b) show the noise immunity and classification sensitivity characteristics of the single-channel AlexNet and dual-channel AlexNet networks, respectively. The single-channel AlexNet network only uses the second-order difference of the far-field spatial image as input, while the dual-channel AlexNet network uses the second-order difference of the far-field aerial images and its first-order lateral gradient as input. From the results shown in figure 8, we can see that the single-channel and dual-channel AlexNet networks have the same powerful performance for the cutting-line defect, the particle defect, and the X-bridge defect, and the classification accuracy of the three types of defects reaches 100%. For the Y-bridge defect, the defect classification accuracy of the dual-channel AlexNet network is significantly higher than the corresponding results of the single-channel AlexNet network, and this phenomenon always occurs in all signal-to-noise ratio situations shown in figure 8(a). As the defect size shrinks from 120 nm to 15 nm, the classification accuracy of the first three types of defects is always close to 100%. Only the classification accuracy of X-bridge defects changes. In most defect situations shown in figure 8(b), the defect classification accuracy of the dual-channel AlexNet network is higher than that of the single-channel AlexNet network. The opposite situations occur only in the 30 nm and 20 nm size defect classification situations. The reason for this phenomenon is that the Y-bridge defect is easily mixed with special particle defects

at the same location, thereby reducing the accuracy of defect classification.

The classification accuracy shown in figure 8 is only for intelligent classification of the second-order difference of the far-field spatial image of a periodic unit and its first-order gradient. If the simulation area is expanded to a 2×2 supercell structure, the dual-channel AlexNet network can demonstrate 100% accuracy in the defect classification experiments. The root cause is that expanding the simulation area can increase the size of the training set, and a richer training set can significantly improve the defect classification characteristics of the AlexNet network.

4. Conclusions

This study proposed a form birefringence-breaking imaging method that overcomes the limitations of conventional bright-field inspection technique in its weak defect classification capabilities, enabling the morphology sensing for deep subwavelength patterned defects in a non-destructive, fast, label-free, convenient to be integrated, and straightforward manner. The method adopts a second-order differential between the aerial images of the defect-contained and the defect-free nanostructures under the two orthogonal polarization illuminations to capture the asymmetrical perturbation in the form-birefringence scattering behaviors of the original nanostructure, which could highlight patterned defects' morphological differences. Using the series simulations based on the self-developed vector imaging model and inspection experiments based on the self-built polarization microscopy, the feasibility and effectiveness of the proposed method in detecting deep subwavelength defects are demonstrated. In particular, sensitivity simulations on various defects with feature sizes less than $\lambda/18$ nm confirm the adaptability and extensibility of the proposed method to the deep-subwavelength defects.

On this basis, an intelligent classification algorithm based on a dual-channel AlexNet convolutional neural network with the second-order differential and its transverse gradient images as the input has been proposed, which stabilizes the classification accuracy of $\lambda/16$-sized defects with highly similar features at more than 90%. The classification accuracy of less than 100% can be attributed to the input pattern just corresponding to a single two-dimensional periodic unit structure, which would essentially limit the size of the training set. With the input pattern size increasing to a 2×2 supercell periodic unit, the classification accuracy of various patterned defects can be improved to 100%.

In fact, the commonly used die-to-die intensity differential pattern is usually very close to the Airy disk, losing the correlation with the defect morphology, which makes the conventional bright-field microscopy technology only have constrained detection sensitivity and meaningless classification capabilities in defect inspection. While the proposed method breaks down the traditional framework of only highlighting the peak in the intensity difference image, and takes the lead in focusing on the spatially distributed polarization responses of the patterned defect, which gives it far better defect identification and classification capabilities than traditional bright field detection technology. In summary, the work will provide a new but easy-to-operate method for detecting and classifying deep-subwavelength defects in patterned wafers or photomasks, which thus endows current online inspection equipment with more missions in advanced IC manufacturing. Considering that the proposed method can be readily and cheaply integrated into current bright-field inspection platforms, it is possible to use as few high-resolution review SEMs as possible in advanced IC manufacturing, which finally leads to the chips' yield improvement without losing productivity. Besides, the quasi-visualizable and label-free detection of nanoscale objects empowered by the form birefringence-breaking imaging framework has also opened up a new route for defect inspections.

Data availability statement

The data that support the findings of this study are available from the corresponding author upon request.

Acknowledgment

This work was funded by National Natural Science Foundation of China (Grant Nos. 52130504, 52305577, and 52175509), the Key Research and Development Plan of Hubei Province (Grant No. 2022BAA013), the Major Program (JD) of Hubei Province (Grant No. 2023BAA008-2), the Interdisciplinary Research Program of Huazhong University of Science and Technology (2023JCYJ047), the Innovation Project of Optics Valley Laboratory (Grant No. OVL2023PY003), the Postdoctoral Fellowship Program (Grade B) of China Postdoctoral Science Foundation (Grant No. GZB20230244), and the fellowship from the China Postdoctoral Science Foundation (2024M750995). The authors acknowledge the Experiment Center for Advanced Manufacturing and Technology in the School of Mechanical Science & Engineering of HUST for assistance in the fabrications and SEM characterization of samples. Besides, the authors would like to thank Dr David H Wei and Dr Xianhua Ke for useful discussions and comments.

Conflict of interest

The authors declare no conflicts of interest.

Author contribution

Jiamin Liu: Conceptualization, Data curation, Formal analysis, Investigation, Methodology, Software, Visualization, Funding, Writing—original draft, Writing—reviewing & editing.

Jinlong Zhu: Conceptualization, Data curation, Formal analysis, Investigation, Methodology, Validation, Funding acquisition, Writing—reviewing & editing.

Zhe Yu: Data curation, Investigation, Visualization, Writing—reviewing & editing.

Xianrui Feng: Data curation, Software, Investigation, Writing—reviewing & editing.

Zedi Li: Data curation, Formal analysis, Investigation, Writing—reviewing & editing.

Lei Zhong: Data curation, Software, Investigation, Writing—reviewing & editing.

Jinsong Zhang: Formal analysis, Formal analysis, Investigation, Writing—reviewing & editing.

Honggang Gu: Software, Visualization, Investigation, Writing—reviewing & editing

Xiuguo Chen: Formal analysis, Visualization, Investigation, Writing—reviewing & editing

Hao Jiang: Conceptualization, Investigation, Methodology, Supervision, Funding acquisition, Writing—reviewing & editing.

Shiyuan Liu: Conceptualization, Investigation, Methodology, Project administration, Supervision, Funding acquisition, Writing—reviewing & editing.

ORCID iDs

Jinlong Zhu https://orcid.org/0000-0002-5723-2879
Xiuguo Chen https://orcid.org/0000-0002-7067-5084
Shiyuan Liu https://orcid.org/0000-0002-0756-1439

References

[1] Chen Y Q, Shu Z W, Zhang S, Zeng P, Liang H K, Zheng M J and Duan H G 2021 Sub-10 nm fabrication: methods and applications *Int. J. Extrem Manuf.* **3** 032002
[2] Lian Y G 2023 *Semiconductor Microchips and Fabrication: A Practical Guide to Theory and Manufacturing* (Wiley-IEEE Press) pp 109–270
[3] Smith B W and Suzuki K 2020 *Microlithography: Science and Technology* 3rd edn (CRC Press) pp 1–40
[4] Tigelaar H 2020 *How Transistor Area Shrank by 1 Million Fold* (Springer) pp 7–19
[5] Orji N G, Badaroglu M, Barnes B M, Beitia C, Bunday B D, Celano U, Kline R J, Neisser M, Obeng Y and Vladar A E 2018 Metrology for the next generation of semiconductor devices *Nat. Electron.* **1** 532–47
[6] Kamaei S, Liu X, Saeidi A, Wei Y F, Gastaldi C, Brugger J and Ionescu A M 2023 Ferroelectric gating of two-dimensional semiconductors for the integration of steep-slope logic and neuromorphic devices *Nat. Electron.* **6** 658–68
[7] Chen T Y *et al* 2023 All-analog photoelectronic chip for high-speed vision tasks *Nature* **623** 48–57
[8] Wu H, Huang Y A, Xu F, Duan Y Q and Yin Z P 2016 Energy harvesters for wearable and stretchable electronics: from flexibility to stretchability *Adv. Mater.* **28** 9881–919
[9] IEEE 2020 *International Roadmap for Devices and Systems (IRDS^{TM}) 2020 Edition: Application Benchmarking Chapter* (IEEE Press) pp 1–35 (available at: https://irds.ieee.org/editions/2020)
[10] Zhu J L, Liu J M, Xu T L, Yuan S, Zhang Z X, Jiang H, Gu H G, Zhou R J and Liu S Y 2022 Optical wafer defect inspection at the 10 nm technology node and beyond *Int. J. Extrem Manuf.* **4** 032001
[11] Nguyen D T, Mun S, Park H, Jeong U, Kim G H, Lee S, Jun C S, Sung M M and Kim D 2022 Super-resolution fluorescence imaging for semiconductor nanoscale metrology and inspection *Nano Lett.* **22** 10080–7
[12] Yuan T, Ramadan S Z and Bae S J 2011 Yield prediction for integrated circuits manufacturing through hierarchical Bayesian modeling of spatial defects *IEEE Trans. Reliab.* **60** 729–41
[13] Zhou R J, Edwards C, Popescu G and Goddard L L 2015 Semiconductor defect metrology using laser-based quantitative phase imaging *Proc. SPIE* **9336** 93361I
[14] Zhu J L, Liu Y A, Yu X, Zhou R J, Jin J M and Goddard L L 2019 Sensing sub-10 nm wide perturbations in background nanopatterns using optical pseudoelectrodynamics microscopy (OPEM) *Nano Lett.* **19** 5347–55
[15] Nakagaki R, Honda T and Nakamae K 2009 Automatic recognition of defect areas on a semiconductor wafer using multiple scanning electron microscope images *Meas Sci. Technol.* **20** 075503
[16] Church J and Meli L 2022 Throughput vs. yield: reviewing the metrology needs for stochastics-aware process window analysis (SA-PWA) *Proc. SPIE* **12053** 1205306
[17] Crimmins T F 2010 Defect metrology challenges at the 11-nm node and beyond *Proc. SPIE* **7638** 76380H
[18] Yoon J W, Ma S M, Kim G P, Kang Y, Hahn J, Kwon O J, Kim K and Song S H 2018 Nanophotonic identification of defects buried in three-dimensional NAND flash memory devices *Nat. Electron.* **1** 60–67
[19] Nakazawa T and Kulkarni D V 2018 Wafer map defect pattern classification and image retrieval using convolutional neural network *IEEE Trans. Semicond. Manuf.* **31** 309–14
[20] Ma Z Y and Seiler D G 2017 *Metrology and Diagnostic Techniques for Nanoelectronics* (Pan Stanford Publishing Pte. Ltd) pp 589–626
[21] Barnes B M, Goasmat F, Sohn M Y, Zhou H, Vladár A E and Silver R M 2015 Effects of wafer noise on the detection of 20-nm defects using optical volumetric inspection *J. Micro/ Nanolithogr. MEMS MOEMS* **14** 014001
[22] Cho S, Lee J, Kim H, Lee S, Ohkubo A, Lee J, Kim T, Bae S and Joo W 2018 Super-contrast-enhanced darkfield imaging of nano objects through null ellipsometry *Opt. Lett.* **43** 5701–4
[23] Edwards C *et al* 2014 Diffraction phase microscopy: monitoring nanoscale dynamics in materials science *Appl. Opt.* **53** G33–G43
[24] Huo P C *et al* 2020 Photonic spin-multiplexing metasurface for switchable spiral phase contrast imaging *Nano Lett.* **20** 2791–8
[25] Chen C, Chen X G, Xia Z W, Shi J C, Sheng S, Qiao W and Liu S Y 2022 Characterization of pixelated nanogratings in 3D holographic display by an imaging Mueller matrix ellipsometry *Opt. Lett.* **47** 3580–3
[26] Gottlieb D and Arteaga O 2021 Mueller matrix imaging with a polarization camera: application to microscopy *Opt. Express* **29** 34723–34
[27] Barnes B M, Sohn M Y, Goasmat F, Zhou H, Vladár A E, Silver R M and Arceo A 2013 Three-dimensional deep sub-wavelength defect detection using $\lambda = 193$ nm optical microscopy *Opt. Express* **21** 26219–26
[28] Virk K S 2021 Fast computation of scattering by isolated defects in periodic dielectric media *J. Opt. Soc. Am.* B **38** 1763–75
[29] Purandare S, Zhu J L, Zhou R J, Popescu G, Schwing A and Goddard L L 2019 Optical inspection of nanoscale structures using a novel machine learning based synthetic image generation algorithm *Opt. Express* **27** 17743–62
[30] Sentenac A, Chaumet P C and Belkebir K 2006 Beyond the Rayleigh criterion: grating assisted far-field optical diffraction tomography *Phys. Rev. Lett.* **97** 243901
[31] O'Callahan B T, Park K D, Novikova I V, Jian T Y, Chen C L, Muller E A, El-Khoury P Z, Raschke M B and Scott Lea A 2020 In liquid infrared scattering scanning near-field optical

microscopy for chemical and biological nanoimaging *Nano Lett.* **20** 4497–504
[32] Westphal V, Rizzoli S O, Lauterbach M A, Kamin D, Jahn R and Hell S W 2008 Video-rate far-field optical nanoscopy dissects synaptic vesicle movement *Science* **320** 246–9
[33] Rust M J, Bates M and Zhuang X W 2006 Sub-diffraction-limit imaging by stochastic optical reconstruction microscopy (STORM) *Nat. Methods* **3** 793–5
[34] Zhou R J, Edwards C, Arbabi A, Popescu G and Goddard L L 2013 Detecting 20 nm wide defects in large area nanopatterns using optical interferometric microscopy *Nano Lett.* **13** 3716–21
[35] Bhaduri B, Edwards C, Pham H, Zhou R J, Nguyen T H, Goddard L L and Popescu G 2014 Diffraction phase microscopy: principles and applications in materials and life sciences *Adv. Opt. Photonics* **6** 57–119
[36] Hong X, van Dijk E M P H, Hall S R, Götte J B, van Hulst N F and Gersen H 2011 Background-free detection of single 5 nm nanoparticles through interferometric cross-polarization microscopy *Nano Lett.* **11** 541–7
[37] Miles B T, Greenwood A B, Patton B R and Gersen H 2016 All-optical method for characterizing individual fluorescent nanodiamonds *ACS Photonics* **3** 343–8
[38] Miles B T, Robinson E C, van Dijk E M H P, Lindsay I D, van Hulst N F and Gersen H 2015 Sensitivity of interferometric cross-polarization microscopy for nanoparticle detection in the near-infrared *ACS Photonics* **2** 1705–11
[39] Zhu J L, Zhou R J, Zhang L N, Ge B L, Luo C X and Goddard L L 2019 Regularized pseudo-phase imaging for inspecting and sensing nanoscale features *Opt. Express* **27** 6719–33
[40] Barnes B M, Henn M A, Sohn M Y, Zhou H and Silver R M 2019 Assessing form-dependent optical scattering at vacuum- and extreme-ultraviolet wavelengths of nanostructures with two-dimensional periodicity *Phys. Rev. Appl.* **11** 064056
[41] Feng L, Liu Z W, Lomakin V and Fainman Y 2010 Form birefringence metal and its plasmonic anisotropy *Appl. Phys. Lett.* **96** 041112
[42] Singh A, Sharma G, Ranjan N, Mittholiya K, Bhatnagar A, Singh B P, Mathur D and Vasa P 2018 Controlling material birefringence in sapphire via self-assembled, sub-wavelength defects *Appl. Phys.* B **124** 20
[43] Xu F, Tyan R C, Sun P C, Fainman Y, Cheng C C and Scherer A 1996 Form-birefringent computer-generated holograms *Opt. Lett.* **21** 1513–5
[44] Schonbrun E, Seo K and Crozier K B 2011 Reconfigurable imaging systems using elliptical nanowires *Nano Lett.* **11** 4299–303
[45] Zhao X, Alizadeh M H and Reinhard B M 2017 Generating optical birefringence and chirality in silicon nanowire dimers *ACS Photonics* **4** 2265–73
[46] Davis T J, Vernon K C and Gómez D E 2009 Designing plasmonic systems using optical coupling between nanoparticles *Phys. Rev.* B **79** 155423
[47] Mishchenko M I, Travis L D and Lacis A A 2002 *Scattering, Absorption, and Emission of Light by Small Particles* (Cambridge University Press) pp 67–174
[48] Mayergoyz I D, Fredkin D R and Zhang Z Y 2005 Electrostatic (plasmon) resonances in nanoparticles *Phys. Rev.* B **72** 155412
[49] Liu J J, Guo C, Li W and Fan S H 2022 Thermal photonics with broken symmetries *eLight* **2** 25
[50] Born M and Wolf E 2016 *Principles of Optics: Electromagnetic Theory of Propagation, Interference and Diffraction of Light* 7th edn (Cambridge University Press) pp 580–613
[51] Rodríguez-Lara B M, El-Ganainy R and Guerrero J 2018 Symmetry in optics and photonics: a group theory approach *Sci. Bull.* **63** 244–51
[52] Nativ A, Feldman H and Shaked N T 2018 Wafer defect detection by a polarization-insensitive external differential interference contrast module *Appl. Opt.* **57** 3534–8
[53] Krizhevsky A, Sutskever I and Hinton G E 2017 ImageNet classification with deep convolutional neural networks *Commun. ACM* **60** 84–90
[54] Minhas R A, Javed A, Irtaza A, Mahmood M T and Joo Y B 2019 Shot classification of field sports videos using AlexNet convolutional neural network *Appl. Sci.* **9** 483
[55] Attota R and Silver R 2012 Optical microscope angular illumination analysis *Opt. Express* **20** 6693–702
[56] Fujiwara H 2007 *Spectroscopic Ellipsometry: Principles and Applications* (Wiley) pp 63–154
[57] Goodman J W 2017 *Introduction to Fourier Optics* 4th edn (W. H. Freeman and Company) pp 30–145
[58] Wong A K K 2005 *Optical Imaging in Projection Microlithography* (SPIE Press)
[59] Golani O, Dolev I, Pond J and Niegemann J 2016 Simulating semiconductor structures for next-generation optical inspection technologies *Opt. Eng.* **55** 025102
[60] Huang F M and Zheludev N I 2009 Super-resolution without evanescent waves *Nano Lett.* **9** 1249–54
[61] Gonzalez R C and Woods R E 2018 *Digital Image Processing* 4th edn (Pearson Education Ltd) pp 47–83
[62] Crimmins T F 2011 Wafer noise models for defect inspection *Proc. SPIE* **7971** 79710E
[63] van Dam D, Abujetas D R, Paniagua-Domínguez R, Sánchez-Gil J A, Bakkers E P A M, Haverkort J E M and Rivas J G 2015 Directional and polarized emission from nanowire arrays *Nano Lett.* **15** 4557–63